

# Identification of PPA1 inhibitor candidates for potential repurposing in cancer medicine

Muratcan Menteş<sup>1</sup> | Cihangir Yandım<sup>1,2</sup> 

<sup>1</sup>Department of Genetics and Bioengineering, Faculty of Engineering, İzmir University of Economics, Balçova, İzmir, Turkey

<sup>2</sup>İzmir Biomedicine and Genome Center (IBG), Dokuz Eylül University Health Campus, Inciralti, İzmir, Turkey

## Correspondence

Cihangir Yandım

Email: [cihangir.yandim@ieu.edu.tr](mailto:cihangir.yandim@ieu.edu.tr) and [cyandim@gmail.com](mailto:cyandim@gmail.com)

## Abstract

Inorganic pyrophosphatase 1 (PPA1) is pivotal to cellular metabolism as it facilitates the hydrolysis of PPi—a by-product of various metabolic processes that influence cell growth and differentiation. Overexpression of PPA1 enzyme has been linked to diminished patient survival and was shown to influence tumor cell dynamics, thereby positioning it as a potential therapy target for a variety of cancers including colorectal cancer, diffuse large B-cell lymphoma, and lung adenocarcinoma. Despite this therapeutic promise, there are no known inhibitors of PPA1 as of today. In this study, we searched for potential PPA1 inhibitors using a molecular docking screen of 30 470 compounds with a history of clinical trials and/or US Food and Drug Administration approval. We specifically targeted the active pocket that coincides with the established catalytic domain. Our screen identified promising hits, which we further subjected to ADMET (absorption, distribution, metabolism, excretion, and toxicity) filtering. Subsequent molecular dynamics (MD) analyses were conducted on devazepide, quinotolast, and tarazepide—the three substances that successfully navigated all filters. MD analyses reinforced the stability of the protein-ligand complexes and confirmed ligand binding, as substantiated by our root mean square deviation, radius of gyration and secondary structures of proteins analyses. Furthermore, Molecular Mechanics Poisson-Boltzmann Surface Area calculations post-MD identified devazepide and quinotolast as showing higher binding affinities; being supported by principal component analysis, free energy landscape, and dynamic cross-correlation matrix results. Overall, our study reveals devazepide and quinotolast as potential candidates

**Abbreviations:** ACPYPE, antechamber python parser interface; ADMET, absorption, distribution, metabolism, excretion and toxicity; ATP, adenosine triphosphate; cAMP, cyclic AMP, adenosine 3',5'-cyclic monophosphate; DCCM, dynamic cross-correlation matrix; DOPE, discrete optimised protein energy; DSSP, define secondary structures of proteins; FDA, US Food and Drug Administration; FEL, free energy landscape; GTP, guanosine triphosphate; LINCS, linear constraint solver; MD, molecular dynamics; mmPBSA, molecular mechanics poisson-Boltzmann Surface Area; NPT, constant number of particles, system pressure, and temperature; NVT, constant number of particles, system volume, and temperature; PCA, principal component analysis; PDB, protein data bank; Pi, inorganic phosphate; PME, particle Mesh Ewald; PPA1, inorganic pyrophosphatase 1; PPi, inorganic pyrophosphate; Rg, radius of gyration; RMSD, root mean square deviation; RMSF, root mean square fluctuation; SEM, standard error of the mean; SMILES, simplified molecular input line entry system.

This is an open access article under the terms of the Creative Commons Attribution License, which permits use, distribution and reproduction in any medium, provided the original work is properly cited.

© 2023 The Authors. *Journal of Cellular Biochemistry* published by Wiley Periodicals LLC.

for PPA1 inhibition which could be considered for repurposing studies that need further experimental validation. These results not only reveal a potential for clinical repurposing for PPA1 inhibition but they also offer valuable insights into the development of future compounds for targeting the crucial PPA1 enzyme.

**KEYWORDS**

cancer, drug screen, inhibitor, molecular docking, molecular dynamics, phosphate metabolism, PPA1, repurposing

**1 | INTRODUCTION**

Phosphate is one of the most prevalent elements in the human body, accounting for approximately 1% of total body mass.<sup>1</sup> Phosphate plays multiple roles in the regulation of cellular processes, including membrane formation and energy conversion, signal transduction, as well as gene expression.<sup>2,3</sup> The maintenance of phosphate is highly important for the body and the dysregulation of phosphate metabolism can result in the pathogenesis of various diseases<sup>4</sup> including cancer.<sup>5</sup> In cells, pyrophosphatases play a significant role in converting inorganic PPI, which is generated as a by-product of many metabolic reactions,<sup>6</sup> to inorganic phosphate (Pi) through hydrolysis (Figure 1, lower middle panel).<sup>7</sup> Two types of family I pyrophosphatases are

found in humans: inorganic pyrophosphatase 1 (PPA1; 289 aa) and -2 (PPA2; 305 aa).<sup>8</sup> PPA1 is present in all human tissues and plays a more prominent role than PPA2.<sup>9</sup>

PPA1 exerts a wide range of functions including lipid metabolism, bone formation, collagen synthesis,<sup>10</sup> DNA synthesis, and neurite growth.<sup>11</sup> It indirectly regulates pathways involving key cancer-related proteins such as p53, β-catenin, Bcl<sup>-2</sup>, and caspase-3 through directly dephosphorylating c-Jun N-terminal kinase 1 (JNK), thereby controlling cell proliferation and apoptosis (Figure 1).<sup>12</sup> PPA1 also indirectly activates the PI3K pathway<sup>13</sup> which is heavily emphasized in cancer. In line with these, PPA1 expression has been notably reported to be upregulated in various types of cancer, such as colorectal cancer,<sup>12,14,15</sup> diffuse large B-cell lymphoma,<sup>16</sup>

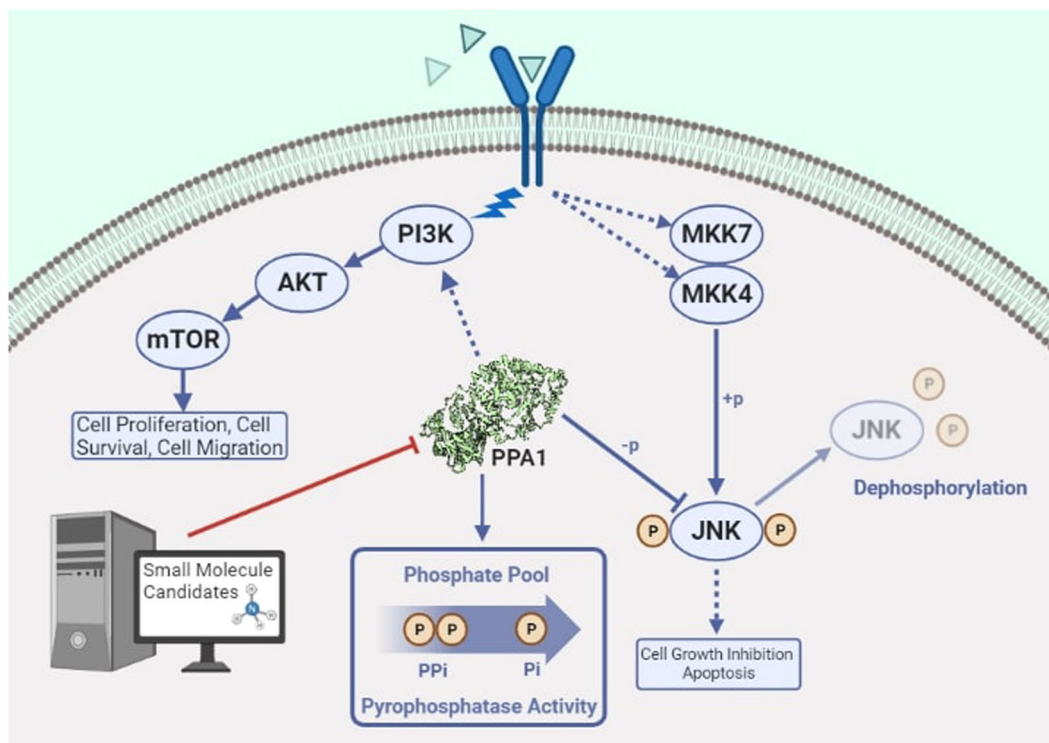


**FIGURE 1** An overview of PPA1 function in intracellular pathways. PPA1, inorganic pyrophosphatase 1.

lung adenocarcinoma,<sup>17,18</sup> prostate cancer,<sup>19</sup> hepatocellular carcinoma,<sup>20</sup> breast cancer,<sup>21</sup> gastric cancer,<sup>22,23</sup> intrahepatic cholangiocarcinoma,<sup>24</sup> and ovarian cancer.<sup>18,25</sup> Remarkably, survival analyses revealed a negative impact of PPA1 levels on patient survival in nonsmall cell lung cancer,<sup>26</sup> colon adenocarcinoma,<sup>12</sup> and ovarian cancer.<sup>27</sup>

The intriguing relationship between PPA1, cancer and survival prompted scientists to investigate the tantalizing possibility of a potential therapeutic outcome of PPA1 inhibition. As no such inhibitors are known yet, scientists were able to demonstrate its potential use by employing RNA interference mediated knockdown experiments, which resulted in reduced cell proliferation and increased apoptosis in lung and breast cancer cells.<sup>28</sup> Similar outcomes were also seen in diffuse large B-cell lymphoma, with an emphasis on the emerging relationship between PPA1 and p53.<sup>16</sup> There were also promising attempts to inhibit PPA1-related pathways and hence several potentially therapeutic agents such as the JNK inhibitor JNK-IN-8,<sup>29</sup> PI3K inhibitor BKM120,<sup>30</sup> and AKT inhibitor capivasertib<sup>31</sup> were introduced.

Despite the significant biological and patho-physiological implications, there are still no known inhibitors for this pivotal enzyme as of today. In line with the emerging need of PPA1 inhibitors in experimental cancer medicine, the aim of this study was to identify potential competitive inhibitors of PPA1 from a pool of currently available small molecules. For potential repurposing, we focused on named molecules available for sale, which either are of biogenic origin or

reached clinical trials and/or US Food and Drug Administration (FDA) approval. We followed a computational pipeline as given in Figure 2. Initially, we performed a drug pocket analysis with DogSiteScorer<sup>32</sup> and identified only one potential druggable pocket (not shown) that aligns well with the enzyme's catalytical site as reported by Niu et al. in 2021. Targeting this catalytical site, we employed PyRx molecular docking screen system<sup>33</sup> using 30 470 molecules, as obtained from ZINC15 compound library.<sup>34</sup> Small molecules that displayed relatively higher affinity (binding free energy  $\leq -9.5$  kcal/mol) through this process were subjected to absorption, distribution, metabolism, excretion, and toxicity (ADMET) filters, to determine the inhibitor candidates that could reach clinics as fast as possible within a potential repurposing scheme. Successful candidates were then subjected to molecular dynamics (MD) simulations against the catalytical site of PPA1, followed by detailed calculations (principal component analysis [PCA], free energy landscape [FEL], Dynamic Cross-Correlation Matrix [DCCM], define secondary structures of proteins [DSSP] and MM-PBSA analyses).

## 2 | MATERIALS AND METHODS

### 2.1 | Collection of the molecular structures of small molecules

We downloaded 30 470 compounds from the ZINC15 database.<sup>34</sup> To effectively manage the extensive libraries

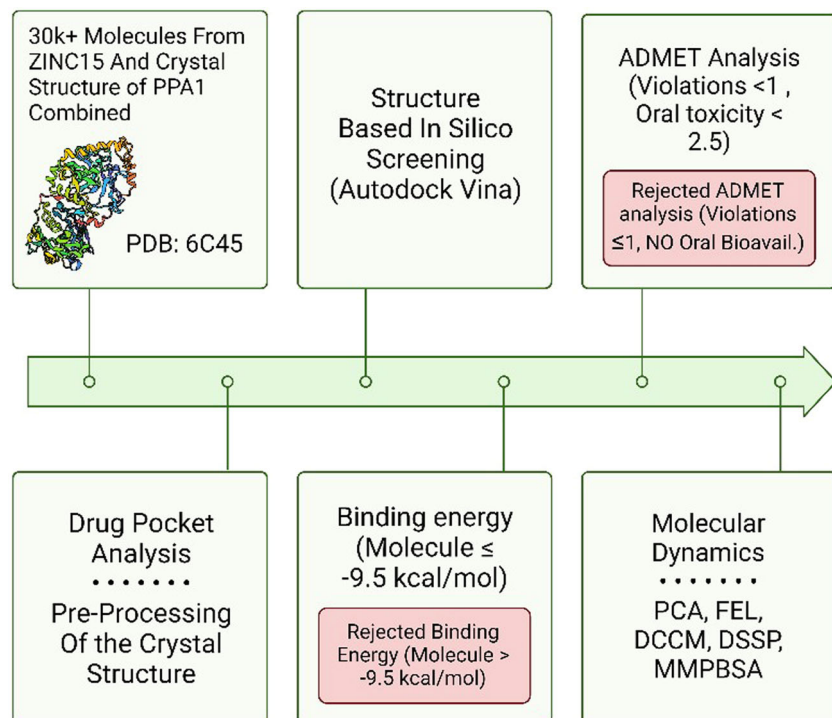


FIGURE 2 Computational workflow of the study.

within this database, we implemented a focused approach by narrowing the investigation to “named” and “commercially available” compounds that are readily accessible in the market and have biogenic origins, currently in clinical trials, historically used in clinical trials and/or approved by FDA; with the purpose of finding hits that could proceed to clinical repurposing as soon as possible. The molecules that we selected were saved in the \*.mol2 file format and imported into the workspace of PyRx docking screen tool.<sup>33</sup> Following this, 10 000 steps of energy minimization with the GAFF and conjugate gradient method were used to optimize the atomic positions of the ligands, ensuring their precision for reliable compound screening.

## 2.2 | Preparation and validation of PPA1 structure

To create a viable PPA1 protein structure, the X-ray diffraction crystal structure of PPA1 (Protein Data Bank [PDB]: 6C45) was obtained from PDB<sup>35</sup> at a resolution of 2.39 Å.<sup>36</sup> To complete the missing residues, we performed homology modeling with the MODELLER software<sup>37</sup> making use of other human PPA1 structures found in the PDB database (7CMO, 7BTN). Created models were verified using the Discrete Optimised Protein Energy [DOPE] algorithm implemented in MODELLER.<sup>38</sup> The best model determined by the DOPE score was selected for further assessment to comprehensively evaluate its structural integrity and accuracy with the help of advanced tools such as ProSA-web<sup>39</sup> and PROCHECK.<sup>40</sup>

## 2.3 | Molecular docking screen and ADMET analysis

To determine targetable pockets in the protein structure, we employed DogSiteScorer, a powerful tool for identifying potential binding sites.<sup>32</sup> This revealed only one suitable ligand pocket, which perfectly aligned with the catalytic domain of PPA1 as Niu et al. previously published (2021). The center of mass of the gridbox for this target site was calculated as 19.55, 60.46, and 37.41 on X, Y, and Z-axes, respectively. To ensure that the docking gridbox encompasses all essential atoms of the catalytic pocket, box dimensions were set to 20 Å × 20 Å × 20 Å. Molecular docking was serially performed using PyRx, which utilizes AutoDock Vina.<sup>33,41</sup> Following the docking process, binding energies were obtained for each candidate molecule. Molecules with a binding free energy ≤ −9.5 kcal/mol were projected into ADMET analysis.

ADMET analysis was conducted using two software tools, SwissADME<sup>42</sup> and AdmetSar.<sup>43,44</sup> The SMILES format of each molecule was extracted from the ZINC15 database. SwissADME, a platform featuring rule-based filters from major pharmaceutical companies, was employed for Lipinski (Pfizer)<sup>45</sup> and Muegge (Bayer)<sup>46</sup> filters. Candidates with one or less filter violation and bioavailability scores ≥ 0.55 were included for further consideration as suggested by previous literature.<sup>47,48</sup> AdmetSar was utilized for further analysis, human intestinal absorption was classified using the HIA data set and framework to establish its viability.<sup>49</sup> Acute oral toxicity was determined based on a model considering toxicity measurements, with lower toxicities (<2.5) indicating promising candidates.<sup>50</sup>

## 2.4 | Molecular dynamics simulations of PPA1-ligand complexes

Promising small molecule candidates underwent MD simulations to gain a better insight into their mode of binding in dynamic motion. Here, we employed GROMACS 2021.3 software<sup>51</sup> using the AMBER99SB-ILDN all-atom force field,<sup>52</sup> which is specifically compatible for our downstream analyses (including Molecular Mechanics Poisson-Boltzmann Surface Area [MMPBSA]) to calculate the outcome of our MD simulations. Our MD simulations were initiated with \*.pdb files obtained as a result of molecular docking. To generate ligand topologies and force field parameters, Acpype (AnteChamber PYthon Parser interfacE) was employed.<sup>53</sup> Protein-ligand complexes were solvated in a cubic box (20 × 20 × 20 Å) using TIP3P water molecules. To maintain system neutrality, solvent molecules were replaced with either Cl<sup>−</sup> or Na<sup>+</sup> ions. Long-range electrostatic interactions were treated using the Particle Mesh Ewald (PME) method. Throughout the simulations, a constant temperature of 300°K was maintained, while the pressure was controlled isotopically at 1 bar using Parrinello-Rahman coupling.<sup>54</sup> The LINCS algorithm<sup>55</sup> was applied to constrain bond lengths, employing a time step of 2 fs. Before the MD run, structures were relaxed through energy minimisation using the steepest descent algorithm for 50 000 steps, followed by 1 ns of equilibration at NVT (constant number of particles, system volume, and temperature) and NPT (constant number of particles, system pressure, and temperature). Subsequently, independent MD simulations were performed, with atomic coordinates saved every 10 ps. The resulting

trajectories were collected for further analysis and characterization.

## 2.5 | Analysis of molecular dynamics trajectories

We performed post MD analyses using the useful tools in the GROMACS kit that includes root mean square deviation (RMSD), root mean square fluctuation (RMSF), hydrogen bond count, FEL, and the radius of gyration (Rg). The estimation of secondary structure mobility was calculated using the dictionary of protein secondary structure method (do\_dssp).<sup>56,57</sup> Results of these analyses were visually represented with Xmgrace. To assess dynamic cross-correlations, the MD-TASK suite<sup>58</sup> was employed. Principal components were calculated using the MODE-TASK PCA script.<sup>59</sup> Molecular Mechanics Poisson-Boltzmann Surface Area (MM-PBSA) approach, which has been utilized as a useful tool in recent publications<sup>60,61</sup> was adopted to approximate the free energy of binding ( $\Delta G$ ) for each candidate molecule using the gmx\_MMPBSA tool.<sup>62,63</sup> Per-residue decomposition analyses during MM-PBSA calculations were performed for all residues located within the proximity of 20 Å from the ligands.

## 3 | RESULTS

### 3.1 | Preparation and validation of PPA1 structure

PPA1 is predominantly found in a homodimeric or tetrameric form.<sup>36</sup> We extracted its homodimeric form from 6C45 PDB structure and performed homology modeling with MODELLER<sup>37</sup> using other human PPA1 structures (PDB:7CMO, 7BTN) to fill the missing aminoacid residues. To generate the best model, we used the Z-dope method, which approximates a protein model's score depending on its composition and size.<sup>38</sup> Among 25 structures produced by MODELLER, the one with lowest normalized Z-dope score ( $-1.36785$ ) was selected for downstream processing and analysis. Once the complete structure of PPA1 dimer was obtained, it was superimposed with 6C45, which resulted in an RMSD of 0.295 Å (Figure 3A). To further verify the validity of our model, we employed ProSA<sup>39</sup> and PROCHECK<sup>40</sup> web-tools. ProSA evaluated the quality of our model by comparing the C $\alpha$  atom positions with similar structures found in the PDB database revealing a Z-score of  $-8.36$  (Figure 3B). We compared our structure with other human PPA1 structures found in the PDB

database, including 6C45, 7CMO, and 7BTN, which produced Z-scores of  $-7.82$ ,  $-7.02$ , and  $-7.66$ , respectively. We also checked if the catalytical pocket could fit into an appropriate docking gridbox (Figure 3C). For further structural evaluation, we generated a Ramachandran plot with PROCHECK. The majority of residues (91.9%) were found in most favored regions, 7.3% in additional allowed regions, 0.8% in generously allowed regions, and none in disallowed regions (Figure 3D). Taken together, these results indicated a well-modeled structure of PPA1, which was ready for further processes and analyses in this study.

### 3.2 | In silico compound screen and ADMET analysis

Molecular docking can be iteratively used to screen a vast number of compounds,<sup>64</sup> thereby enabling the discovery of molecules with potentially high binding affinities against a target protein. In this study, a total of 30 470 compounds sourced from the ZINC15 database<sup>34</sup> were subjected to docking onto the active site of the Chain-A of PPA1.<sup>36</sup> Chain-A was selected as the better-scored chain in the original crystallized structure. Docking was performed using a suitable gridbox configuration, as illustrated in Figure 3C. We employed PyRx virtual screening software,<sup>33</sup> which employs Autodock Vina.<sup>41</sup> The interaction between the ligand and the protein was determined by evaluating the binding free energy (Supporting Information: Table 1). Our virtual screening process was concluded by establishing a threshold of  $\leq -9.50$  kcal/mol. This allowed reducing the number of molecules, selecting only the significant compounds as demonstrated in Table 1.

Following the identification of 12 promising small molecules through molecular docking, their absorption, distribution, metabolism, elimination, and toxicity (ADMET) properties were evaluated using the widely recognized *in silico* ADMET profiling tools, SwissADME<sup>42</sup> and AdmetSar,<sup>43,44</sup> as presented in Table 2. In SwissADME, the Lipinski,<sup>45</sup> and Muegge<sup>46</sup> filters were applied. These filters are well-established indicators that provide valuable insights into a molecule's features, including molecular weight, lipophilicity and rotatable bonds.<sup>47</sup> Additionally, only the molecules that had good Abbott bioavailability scores ( $\geq 0.55$ ) were selected as suggested previously.<sup>47,48</sup> AdmetSar was utilized to assess crucial factors such as human oral bioavailability, intestinal absorption characteristics and acute oral toxicity scores; where a threshold of  $\leq 2.5$  was applied as described before.<sup>50</sup> We focused on candidate hits that could reach clinics easily with fewer potential side effects

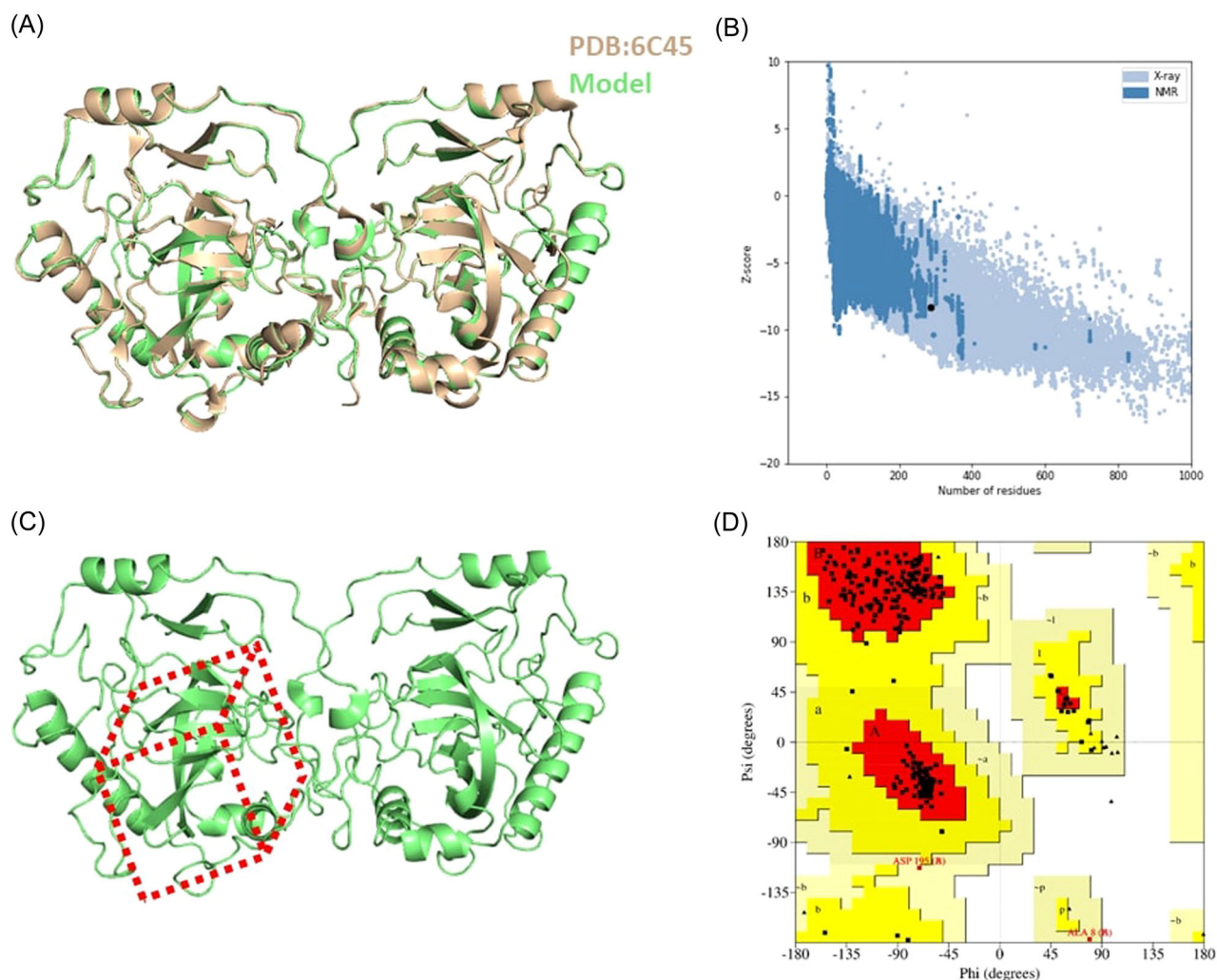


**FIGURE 3** Evaluation of the quality of modeled PPA1 structure. (A) Structural alignment of the current model with the original PDB structure (6C45). (B) The Z-score plot of the model indicating the model's quality in relation to other structures within its range. (C) The placement of the grid box for molecular docking. (D) Ramachandran plot of the processed model. PPA1, inorganic pyrophosphatase 1.

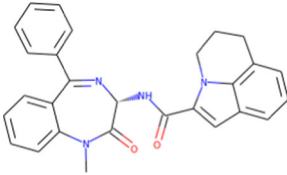
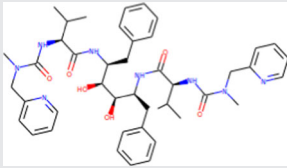
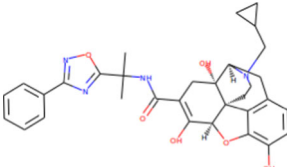
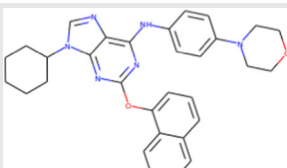
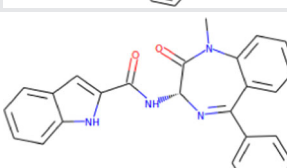
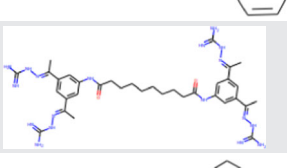
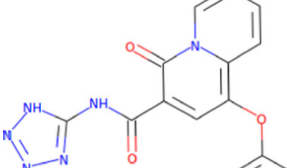
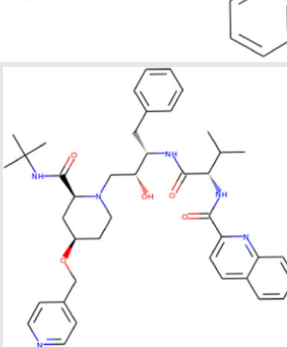
and the aforementioned factors served as eliminative parameters to screen and prioritize candidate molecules.<sup>65</sup> Consequently; three ligands—devazepide, quinotolast and tarazepide—successfully met all the applied filters (given in bold characters in Table 2). To better understand the relationship between the promising ligands and PPA1, we visualized their binding modes using LigPlot+,<sup>66</sup> which allows one to observe the hydrogen bonds and the interacting amino acids (Figure 4). Next, the dynamics of these potential interactions between the selected ligands and PPA1 were analyzed using MD simulations.

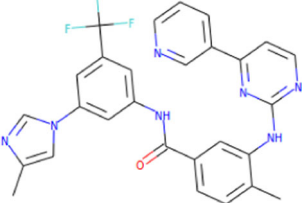
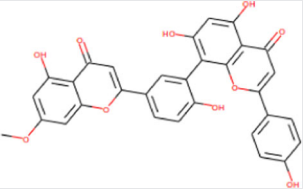
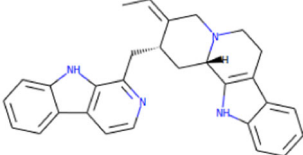
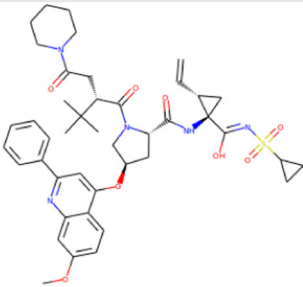
### 3.3 | Molecular dynamics simulations

Stability and dynamics of the most promising small molecule ligands; devazepide, quinotolast and tarazepide,

and their interaction with PPA1 were analyzed with a MD simulation using GROMACS.<sup>51</sup> Upon molecular docking, all three ligands were separately subjected to a 40 ns MD simulation with the PPA1 homodimer at 300°K. The stability of each complex was demonstrated using RMSD of backbone-to-backbone trajectories to see possible backbone shifts. The backbone RMSD values for devazepide, quinotolast and tarazepide complexes reached stability at 20 ns and remained stable for the rest of MD simulation. The RMSD values for Devazepide-PPA1 complex averaged at 0.250 nm, with a standard deviation of 0.031. Similarly, tarazepide-PPA1 complex exhibited an average RMSD of 0.222 nm with a standard deviation of 0.036, while quinotolast-PPA1 complex displayed an average RMSD of 0.306 nm with a standard deviation of 0.045. The results pointed out similar RMSD characteristics for all three compounds in a dynamic relationship with PPA1 (Figure 5A).

**TABLE 1** The outcome of the docking screen as identified molecules and their corresponding binding affinities.

Zinc ID	Compound name	Structure	Binding free energy (kcal/mol)
zinc00002015955	Tarazepide		-10
zinc000085548251	A-77003		-9.9
zinc000100378061	Naldemedine		-9.8
zinc000014806830	Purmorphamine		-9.7
zinc000001847292	Devazepide		-9.6
zinc000072266997	Semapimod		-9.6
zinc000000002018	Quinotolast		-9.5
zinc000003936474	Palinavir		-9.5

Zinc ID	Compound name	Structure	Binding free energy (kcal/mol)
zinc000006716957	Nilotinib		-9.5
zinc000029042407	Sequoiaflavone		-9.5
zinc000030726809	Usambarensine		-9.5
zinc000085537149	Sovaprevir		-9.5

Note: (Molecule structures were taken from the PubChem database).

The  $R_g$  was then evaluated as a measure of compactness and protein structure size.<sup>67</sup> This value is calculated by the distribution of atoms around the protein axis, facilitating the estimation of pressure exerted on a specific location and showing the strength of bonds between two cross-sections. In all inhibitor-protein complexes, we observed similarly stable results (Figure 5B). The  $R_g$  for devazepide-PPA1 complex averaged 2.746 nm with 0.015 standard deviation, the  $R_g$  for tarazepide-PPA1 complex averaged 2.749 nm with 0.012 standard deviation and the  $R_g$  for quinotolast-PPA1 complex averaged 2.750 nm with 0.014. To determine whether PPA1 protein undergoes structural fluctuations, we calculated RMSF. Overall, all protein-ligand complexes exhibited similar behavior with this analysis. The Devazepide-PPA1 complex demonstrated an average RMSF of 0.137 nm, accompanied by a standard deviation of 0.066. In the case of the tarazepide-PPA1 complex, the RMSF averaged at 0.134 nm, with a standard deviation of 0.085. Similarly, the quinotolast-PPA1 complex exhibited an average RMSF of 0.148 nm, with a standard deviation

of 0.066. Peak fluctuation was observed between residues 100 and 120 for all ligands, but tarazepide exhibited a notable increase in fluctuation in this interval (Figure 5C). In contrast to PPA1 protein *per se*, the ligands inside the pocket exhibited a more dynamic behavior. Devazepide and tarazepide underwent a significant change in binding mode at the beginning of the simulation, culminating in a stable state later on. Quinotolast, on the other hand, underwent a considerable change in its binding mode at the 8 ns mark, which was sustained until 28 ns before changing again and remaining at this final state until the end of simulation (Figure 5D). The devazepide complex exhibited an average RMSD of 0.782 nm, with a standard deviation of 0.082. For tarazepide, the average RMSD was 0.504 nm, accompanied by a standard deviation of 0.058. Additionally, the quinotolast complex displayed an average RMSD of 0.435 nm, with a standard deviation of 0.122. The behavior of all ligands were also reflected in hydrogen bond analysis (Figure 5E). Devazepide and tarazepide formed stable hydrogen bonds throughout the



TABLE 2 Evaluation of the ADMET properties of the molecules identified through molecular docking.

ZINC ID	Compound name	ADMET analysis					
		Lipinski filter (Pfizer)	Muegge filter (Bayer)	Bioavailability score	Human oral bioavailability	Acute oral toxicity	Human intestinal absorption
<b>zinc000002015955</b>	<b>Tarazepide</b>	<b>0 violation</b>	<b>0 violation</b>	<b>0.55</b>	+	<b>2.49</b>	+
zinc000085548251	A-77003	3 violations	4 violations	0.17	+	2.16	–
zinc000100378061	Naldemedine	1 violation	1 violation	0.55	–	3.72	+
zinc000014806830	Purmorphamine	1 violation	1 violation	0.55	+	1.77	+
<b>zinc000001847292</b>	<b>Devazepide</b>	<b>0 violation</b>	<b>0 violation</b>	<b>0.55</b>	+	<b>1.92</b>	+
zinc000072266997	Semapimod	3 violations	4 violations	0.17	–	2.81	+
<b>zinc000000002018</b>	<b>Quinotolast</b>	<b>0 violation</b>	<b>0 violation</b>	<b>0.56</b>	+	<b>2.50</b>	+
zinc000003936474	Palinavir	2 violations	3 violations	0.17	–	2.41	+
zinc000006716957	Nilotinib	1 violation	0 violation	0.55	–	2.68	+
zinc000029042407	Sequoiaflavone	1 violation	2 violations	0.55	–	1.81	+
zinc000030726809	Usambarensine	0 violation	1 violation	0.55	–	3.54	+
zinc000085537149	Sovaprevir	2 violations	4 violations	0.17	+	2.78	+

Note: (Substances indicated in bold characters are those that passed all filters).

simulation, whereas quinotolast drifted in hydrogen bond formation at around 8 and 25 ns marks. Among the compounds examined, quinotolast demonstrated the highest count of hydrogen bonds averaging 1.160 throughout the simulation, while devazepide exhibited a relatively lower average of 0.334, and tarazepide achieved the lowest number of H-bonds averaging at 0.011.

### 3.4 | Principal motion and cross correlation analyses on PPA1 upon ligand binding

To further reveal the dynamic response of PPA1 structure upon ligand binding, we utilized PCA, a mathematical method that reduces multidimensional sets of variables to smaller dimensions based on covariance matrices. PCA determines the diffusive characteristics of proteins during various folding phases and calculates atomic displacements in each conformation comprising the trajectory.<sup>68</sup> Here, devazepide was associated with a relatively stable PPA1 structure throughout the simulation, whereas quinotolast exerted some changes on PPA1 structure after the initial quarter of the simulation (Figure 6A). Tarazepide, on the other hand, causes an obvious change in the protein's conformation at later phases of the simulation. The thermodynamics and kinetics of

molecular processes in solution could be inferred by FEL calculations.<sup>69</sup> When FEL calculations were projected onto the PCA graph we obtained earlier, devazepide and quinotolast exhibited their lowest energy states towards the end of the simulation (Figure 6B). However, tarazepide began with the lowest energy state and transitioned to a higher energy state by the end. To further characterize the conformational dynamics of PPA1, we conducted DCCM analysis to see the correlated motions among all amino acids of PPA1 upon ligand binding. DCCM calculates cooperative atomic motions by analyzing the covariance and time correlation of positional fluctuations of atoms within a protein-ligand complex.<sup>70</sup> Upon analyzing the dimer structure, it was observed that PPA1-devazepide complex exhibited the lowest level of correlation, while PPA1-quinotolast complex displayed a less degree of correlation. Conversely, PPA1-tarazepide complex exhibited the highest level of correlation within the structure among all the ligand molecules studied here (Figure 6C). We also analyzed the mobility of secondary structures using the DSSP analysis and we curated structural snapshots from diverse time intervals throughout our MD simulations (0–20–40 ns) and superimposed them onto the original 6C45 structure (Supporting Information: Figure 1). These analyses aimed to understand structural dynamics linked to the interaction between the ligands and PPA1. The results indicated that the presence

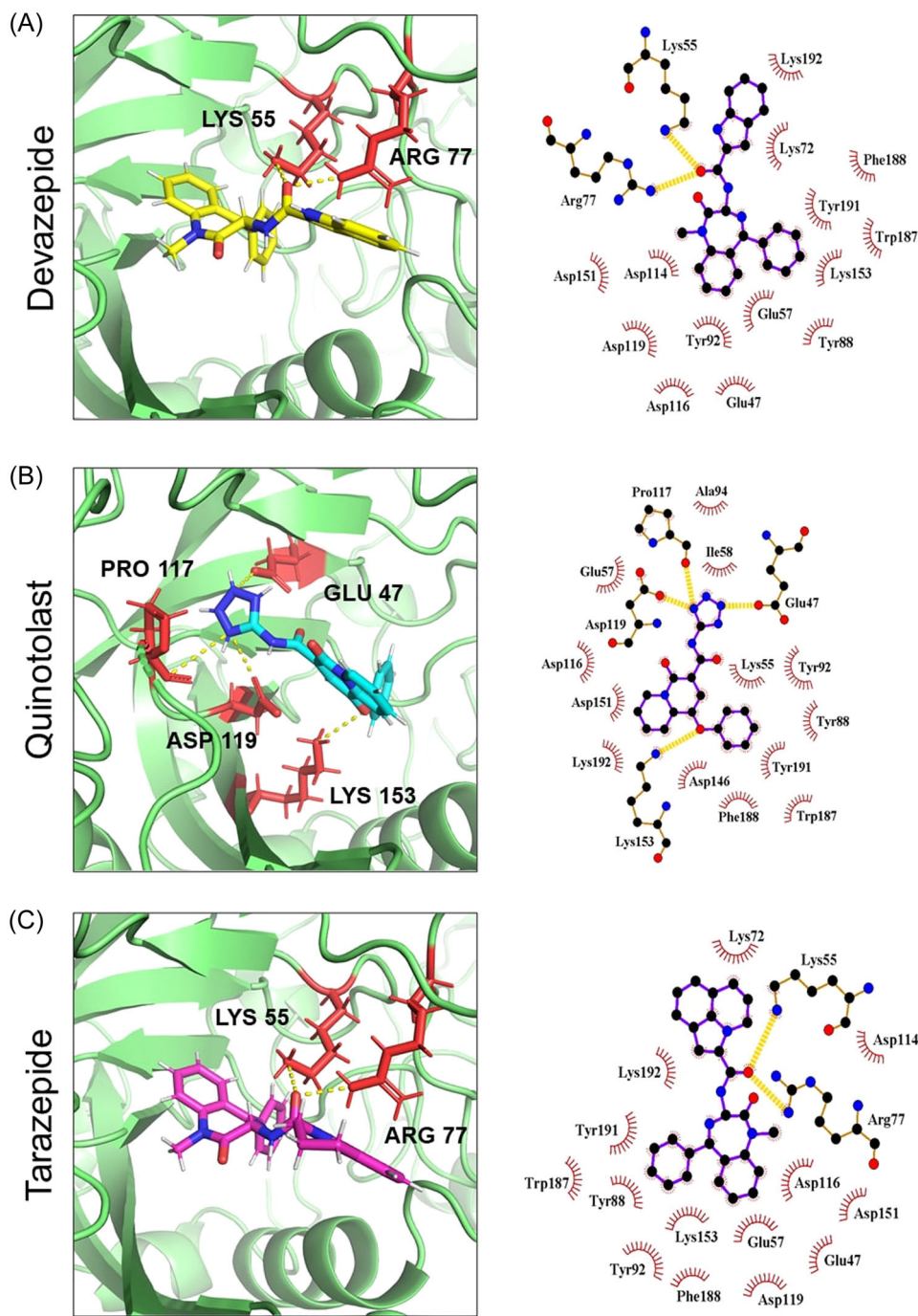


**FIGURE 4** Candidate small molecule inhibitors against PPA1. Docking poses of (A) devazepide, (B) quinotolast, (C) tarazepide (left panel) and 2D illustration of the binding with LigPlot + (right panel). Ligand molecules are shown in contact with the amino acid residues through hydrogen bonds (yellow) and Van der Waals interactions (red). PPA1, inorganic pyrophosphatase 1.

of any molecule did not result in significant conformational changes in PPA1's secondary structure. This could potentially be linked to the compounds' competitive binding behavior, which hinders substrate binding, rather than being solely attributed to inhibition through conformational changes (Supporting Information: Figure 2).

### 3.5 | Binding free energy analyses with MM-PBSA and per-residue decomposition

To determine the average binding affinities of stabilized PPA1 protein-ligand complexes, relatively stable final parts of all trajectories covering the last 10 ns of MD simulations were analyzed (Table 3). This analysis was

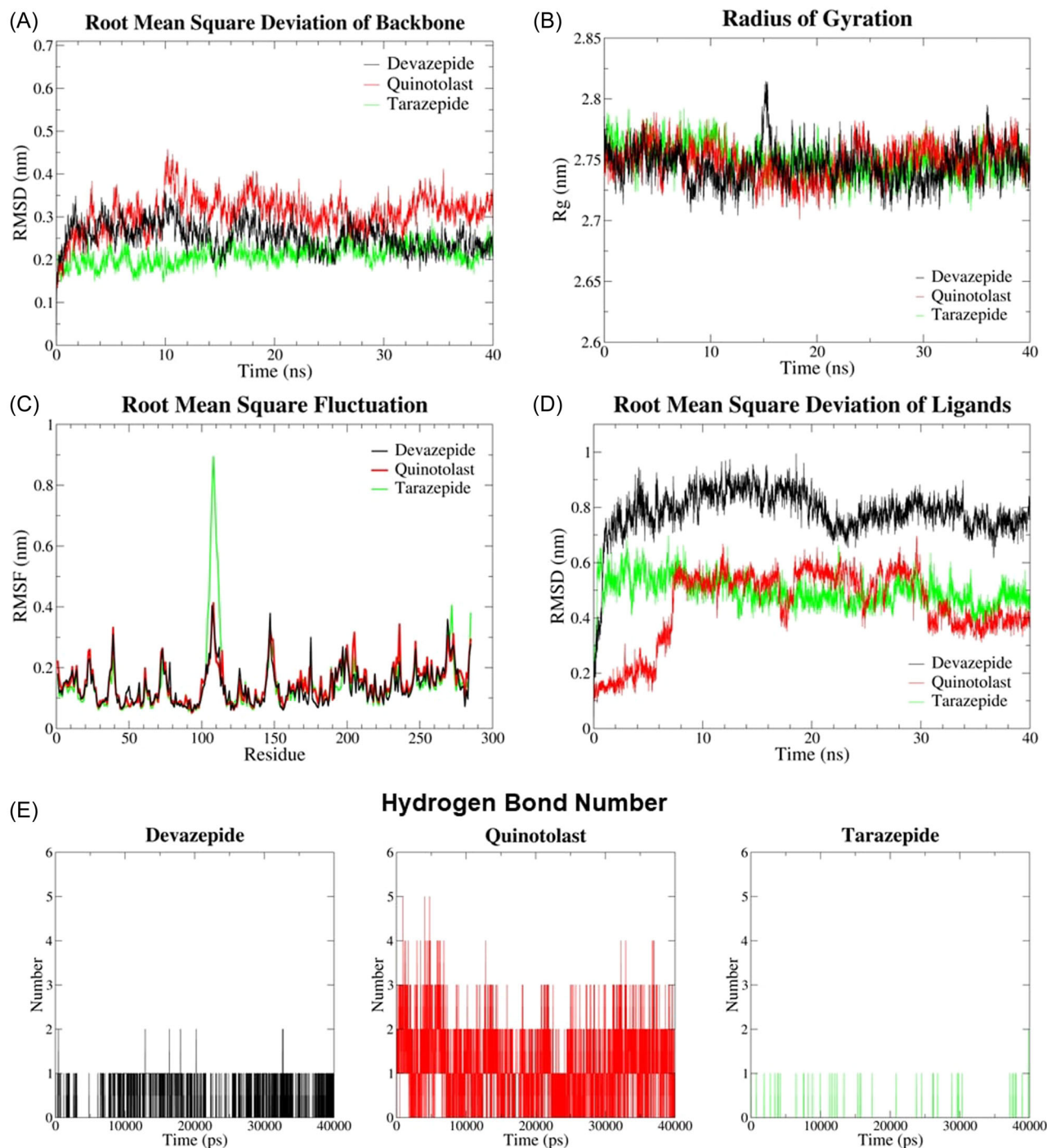


**FIGURE 5** Molecular dynamics analyses to examine the behavior of potential inhibitors of PPA1. (A) Calculation of RMSD values for backbone C $\alpha$  atoms of PPA1 with different ligands over time. (B) Measurement of the radius of gyration (Rg) for all three ligands. (C) Calculation of RMSF values for all ligands along the amino acid residues of PPA1. (D) Calculation of the RMSD values of ligands over time. (E) Intramolecular hydrogen bond formation between PPA1 and; devazepide (black), quinotolast (red), tarazepide (green). PPA1, inorganic pyrophosphatase 1; RMSD, root mean square deviation; RMSF, root mean square fluctuation.

conducted using the MMPBSA calculations.<sup>62,63</sup> Devazepide exhibited the highest binding affinity among all tested compounds, indicating a strong interaction with the target protein. Quinotolast also displayed a similarly high binding affinity, implicating another strong

interaction with PPA1. In contrast, tarazepide displayed a lower binding affinity, suggesting a relatively weaker interaction with PPA1 in dynamic motion.

We also conducted decomposition analyses to determine the contribution of individual amino acid

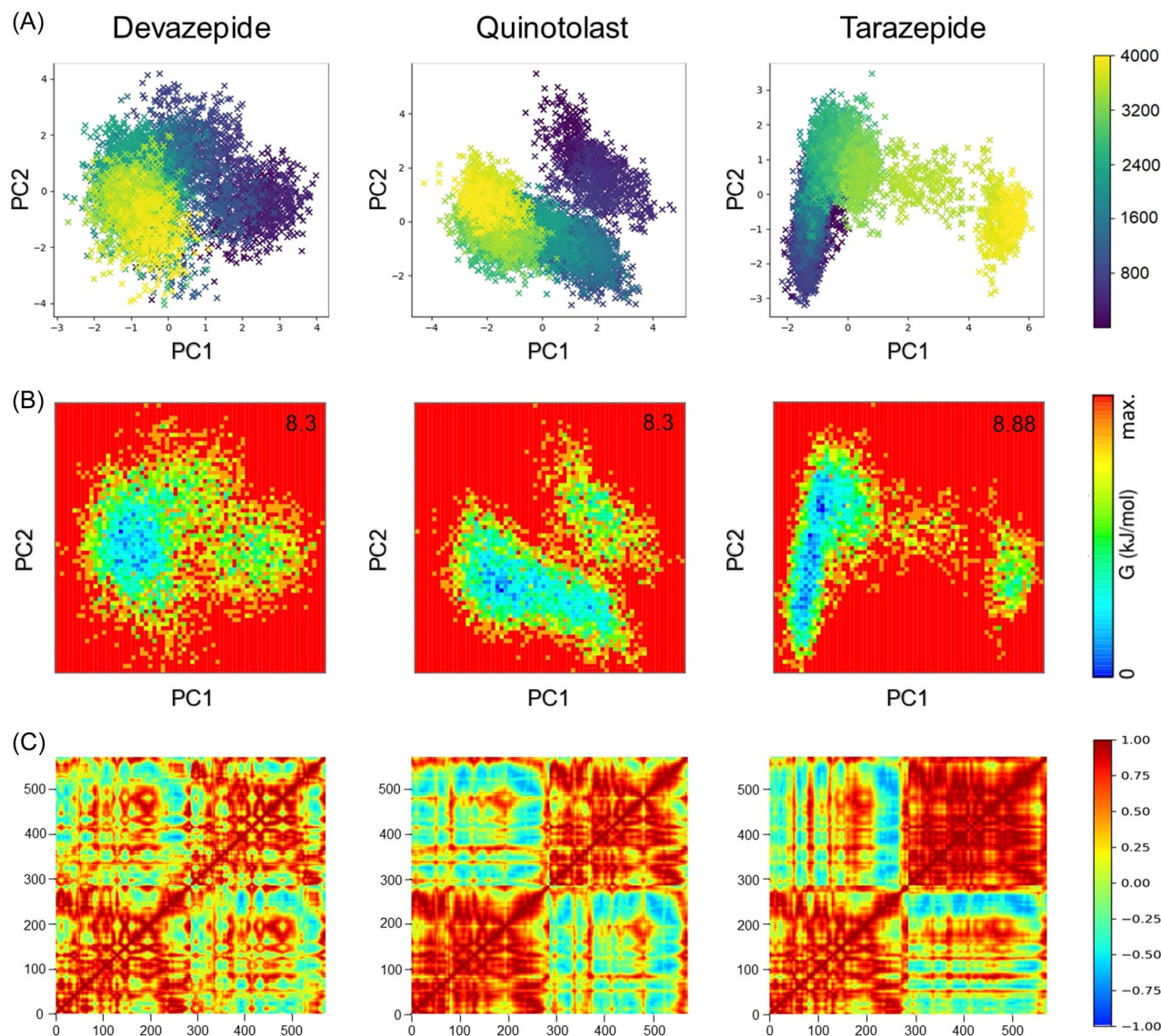


**FIGURE 6** Principal motion and cross-correlation analyses of MD trajectories. (A) Principal component analysis (PCA) where the first frame was highlighted in purple and the last frame was highlighted in yellow. (B) FEL (Free energy landscape) analysis, the function of PC1 and PC2 illustrated by FEL, with the lowest energy state denoted by the blue color and highest with red. (C) DCCM (Dynamic cross-correlation matrix) plots showing dynamic cross-correlation of PPA1 aminoacids. Complete correlation is represented with red color, while complete anti-correlation is represented with blue. MD, molecular dynamics; PPA1, inorganic pyrophosphatase 1.

residues to ligand binding during the MD simulation. Per-residue analysis revealed many interacting residues among which 8 residues exhibited a notable change in free energy ( $\Delta G < -0.5$  kcal/mol) for devazepide whereas 7 residues appeared for quinotolast and tarazepide (Figure 7). Although a large number of residues were affected, the decomposition results for significant residues ( $\Delta G < -0.5$  kcal/mol) for all candidates generally agreed well with the corresponding residues in the molecular docking poses presented in Figure 4 earlier. Among all the ligands, two residues, LYS153 and TRP187, were found to be shared. These residues have varying degrees of impact on different

ligands, with some showing a more significant effect. Devazepide exhibited the highest number of residues that positively influenced the binding, indicating a strong and favorable interaction with PPA1. Compared to devazepide, there were fewer notable residues for quinotolast and tarazepide in this analysis; though with significantly higher binding affinities for certain amino acids such as ASP70 for quinotolast and LYS153 for tarazepide. Moreover, ligand binding to the catalytic domain of PPA1 seems to have minor effects on the stability of this protein when the trajectories are compared to that of ligand-free MD simulations (Supporting Information: Figure 3).

	Devazepide		Quinotolast		Tarazepide	
	Avg	SEM	Avg	SEM	Avg	SEM
VDWAALS	-45.74	0.07	-40.67	0.08	-40.65	0.11
EEL	-2.50	0.09	-306.08	0.66	-9.09	0.08
EPB	22.56	0.10	325.12	0.78	42.07	0.21
ENPOLAR	-4.23	0.00	-4.04	0.00	-4.70	0.01
EDISPER	0.00	0.00	0.00	0.00	0.00	0.00
$\Delta G$ gas	-48.24	0.11	-346.75	0.68	-49.75	0.14
$\Delta G$ solv	18.32	0.09	321.08	0.78	37.36	0.21
$\Delta G$ bind	-29.91	0.11	-25.67	0.24	-12.39	0.18

**TABLE 3** Binding free energies and important attributes of the ligands as calculated from MD trajectories by employing the MMPBSA method.

Abbreviations: Avg, average; MD, molecular dynamics; MMPBSA, Molecular Mechanics Poisson-Boltzmann Surface Area; SEM, standard error of the mean.

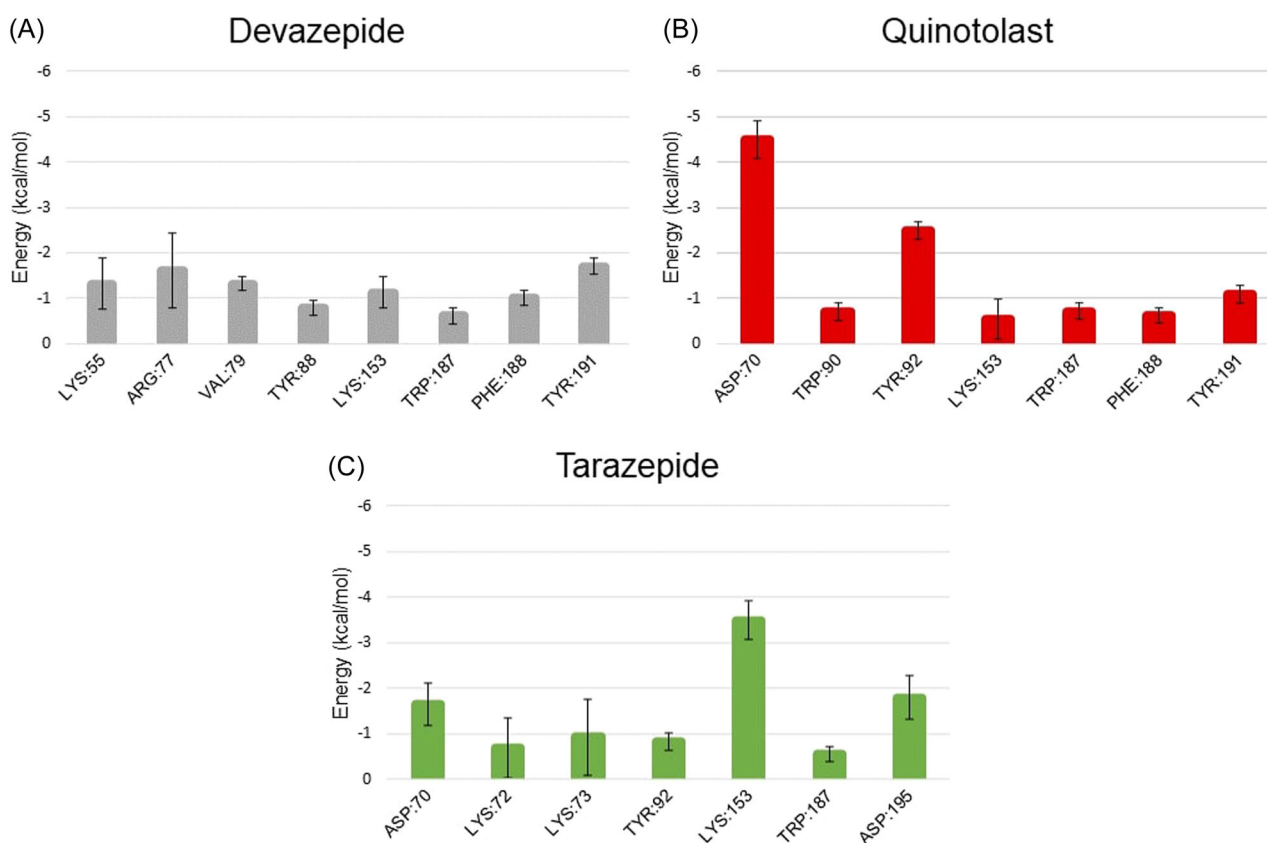


**FIGURE 7** The decomposition analysis of PPA1 residues. (Only the residues with  $\Delta G < -0.5$  kcal/mol were shown). PPA1, inorganic pyrophosphatase 1.

## 4 | DISCUSSION

Given the critical involvement of the PPA1 enzyme in cancer and the absence of its known inhibitors, our objective was to explore small molecule compounds with the potential to interfere with PPA1 activity. We particularly focused our screen on existing compounds

that at least reached clinical trials, with a potential for repurposing strategy that could reach clinics more easily. Our *in silico* investigation revealed three potential repurposing ligands: devazepide, quinotolast, and tarazepide. Devazepide and tarazepide were successful in preclinical analyses and reached clinical stage,<sup>71,72</sup> while quinotolast progressed to regulatory approval for clinical

use in some countries.<sup>73,74</sup> Our MD analyses revealed that the PPA1-ligand complexes exhibited stable behavior with these ligands, as indicated by consistent RMSD backbone and Rg values. The RMSF results exhibited similar fluctuations for all ligands, with the exception of tarazepide displaying greater fluctuation between residues 100–120. These results were in line with PCA and FEL evaluations as well as with MMPBSA calculations followed by decomposition (per-residue) analyses. In particular, devazepide and quinotolast demonstrated greater stability throughout MD and ultimately reached the minimum energy state at the end of MD simulations. Tarazepide, on the other hand, achieved a minimum energy state at the beginning of the simulation followed by a continuous decline as specifically noted in PCA and FEL graphs. DCCM analysis revealed slight differences in the motion of protein-ligand complexes with a notable difference for tarazepide in line with our other results. These observations suggest a compromised binding for tarazepide towards PPA1 in a dynamic simulation as opposed to the earlier docking result. This was also consequently observed in MMPBSA calculations. Devazepide and quinotolast consistently progressed towards the minimum energy complex, maintaining their stability in PPA1-bound form and thereby preserving their high binding affinities.

Despite having similar docking poses, interacting amino acids, and molecular structures, devazepide and tarazepide exhibited a substantial difference in their binding to PPA1 during MD simulations. To gain deeper insight into the underlying causation, an intricate analysis of the pharmacophore attributes of these small molecules was conducted<sup>75</sup> as presented in Supporting Information: Figures 4–6. These attributes offer valuable information about the spatial arrangement of functional groups within the molecules, thereby influencing their biological activities.<sup>76</sup> Furthermore, a comprehensive pharmacophore model was generated to illustrate the conserved features among these ligands, as depicted in Supporting Information: Figure 7.

The pharmacophore features of devazepide and tarazepide were generally similar, agreeing well with our molecular docking results. However, the difference between the binding stabilities of these ligands could be attributed to the presence of an extra H-bond donor in devazepide. This observation aligns well with our other findings, particularly in terms of hydrogen bond formation during MD simulations. Given that hydrogen bonds are regarded as the primary factors contributing to stronger protein-ligand interaction,<sup>77</sup> the presence of the extra H-bond donor in devazepide likely contributes to its favorable stability within PPA1's target binding pocket, thereby enabling it to have a relatively stable affinity.

Similar to devazepide, quinotolast also exhibited this H-bond donor around the same position and overall exhibiting better H-Bond formation capabilities compared to other ligands (Figure 5E). Intriguingly, quinotolast, which is the most active ligand within the binding pocket (Figure 5B), seems to contradict with the hydrogen bond formation. However, the introduction of hydrogen bond donors or acceptors to bolster protein-ligand interactions may not invariably yield heightened binding affinity,<sup>77</sup> and might not necessarily augment the stability of the ligand. Thus, devazepide and quinotolast stand out as inhibitor candidates against PPA1. Devazepide is a cholecystokinin antagonist that targets the neuroactive ligand-receptor interaction, Insulin secretion and pancreatic secretion pathways.<sup>78</sup> It is also worth mentioning that devazepide has primarily been tried as an anti-anxiety medication. Quinotolast is an orally administered mast cell stabilizer and exerts a cytoprotective influence on the gastric mucosa, serving as an agent with antiallergic and antiulcer properties.<sup>79</sup> Considering all, it becomes crucial to seek further clarification in laboratory experiments to ascertain the safety of these drugs in the context of cancer treatment since computations inherently involve certain approximations and simplifications. Ensuring that these calculations correctly reflected the real life applications and, the anticipated and common side effects, including physiological depression or suppression in the case of quinotolast<sup>80</sup> and gallstone toxicity associated with devazepide,<sup>81</sup> should be effectively addressed before attempting to use them for repurposing.

In conclusion, our study aimed to identify potential competitive inhibitors for PPA1, a pivotal protein involved in phosphate metabolism and cancer cell proliferation. Our primary objective was to identify candidate repurposing molecules that have the potential to bypass the lengthy process of de novo drug development. However, the compounds identified here need further experimental validation. Following our initial analyses, three ligands; namely devazepide, quinotolast, and tarazepide, emerged as promising candidates. Each of these compounds did not cause a significant change in the structural conformation of PPA1. Upon conducting a more comprehensive evaluation, tarazepide did not demonstrate satisfactory performance. Therefore, pre-clinical testing is especially warranted for devazepide and quinotolast. To overcome the limitations of our study, further preclinical toxicity/drug interaction analysis would also be invaluable before considering these candidates for PPA1 inhibition. Our MD simulations formed stable complexes within the 40 ns time-frame presented in this study. Still, there is no consensus in the literature on drug discovery in terms of MD simulation

times<sup>82–85</sup> and simulations covering longer time periods would provide deeper insights into the structural dynamics of PPA1 bound by drug candidates.

## AUTHOR CONTRIBUTIONS

**Conceptualization:** Muratcan Menteş and Cihangir Yandım. **Data curation:** Muratcan Menteş and Cihangir Yandım. **Formal analysis:** Muratcan Menteş and Cihangir Yandım. **Investigation:** Muratcan Menteş and Cihangir Yandım. **Methodology:** Muratcan Menteş and Cihangir Yandım. **Project administration:** Cihangir Yandım. **Resources:** Cihangir Yandım. **Software:** Cihangir Yandım. **Supervision:** Cihangir Yandım. **Validation:** Muratcan Menteş and Cihangir Yandım. **Visualization:** Muratcan Menteş and Cihangir Yandım. **Roles/Writing—original draft:** Muratcan Menteş and Cihangir Yandım. **Writing—review and editing:** Cihangir Yandım.

## ACKNOWLEDGMENTS

The high-end computer analyses in this study were performed at TUBITAK ULAKBIM, High Performance and Grid Computing Center (TRUBA Resources). We sincerely thank TUBITAK for providing this platform.

## CONFLICT OF INTEREST STATEMENT

The authors declare no conflict of interest.

## DATA AVAILABILITY STATEMENT

The data that support the findings of this study are available from the corresponding author upon reasonable request.

## ORCID

Cihangir Yandım  <http://orcid.org/0000-0002-2050-6186>

## REFERENCES

- Farrow EG, White KE. Recent advances in renal phosphate handling. *Nat Rev Nephrol.* 2010;6(4):207-217. doi:10.1038/nrneph.2010.17
- Sapio L. Inorganic phosphate in the development and treatment of cancer: a janus bifrons. *World J Clin Oncol.* 2015;6(6):198-201. doi:10.5306/wjco.v6.i6.198
- Takeda E, Taketani Y, Sawada N, Sato T, Yamamoto H. The regulation and function of phosphate in the human body. *Biofactors.* 2004;21(1-4):345-355. doi:10.1002/biof.552210167
- Bergwitz C, Jüppner H. Phosphate sensing. *Adv Chronic Kidney Dis.* 2011;18(2):132-144. doi:10.1053/j.ackd.2011.01.004
- Brown RB, Razzaque MS. Phosphate toxicity and tumorigenesis. *Biochimica et Biophysica Acta.* 2018;1869(2):303-309. doi:10.1016/j.bbcan.2018.04.007
- Kornberg A. Pyrophosphorylases and phosphorylases in biosynthetic reactions. *Adv Enzymol Relat Subj Biochem.* 1957;18:191-240. doi:10.1002/9780470122631.ch5
- Lahti R. Microbial inorganic pyrophosphatases. *Microbiol Rev.* 1983;47(2):169-178. doi:10.1128/mr.47.2.169-178.1983
- Fairchild TA, Patejunas G. Cloning and expression profile of human inorganic pyrophosphatase. *Biochimica et Biophysica Acta.* 1999;1447(2-3):133-136. doi:10.1016/s0167-4781(99)00175-x
- Kajander T, Kellosalo J, Goldman A. Inorganic pyrophosphatases: one substrate, three mechanisms. *FEBS Lett.* 2013;587(13):1863-1869. doi:10.1016/j.febslet.2013.05.003
- Ryan LM, McCarty DJ. Understanding inorganic pyrophosphate metabolism: toward prevention of calcium pyrophosphate dihydrate crystal deposition. *Ann Rheum Dis.* 1995;54(12):939-941. doi:10.1136/ard.54.12.939
- Tezuka Y, Okada M, Tada Y, Yamauchi J, Nishigori H, Sanbe A. Regulation of neurite growth by inorganic pyrophosphatase 1 via JNK dephosphorylation. *PLoS One.* 2013;8(4):e61649. doi:10.1371/journal.pone.0061649
- Wang P, Zhou Y, Mei Q, Zhao J, Huang L, Fu Q. PPA1 regulates tumor malignant potential and clinical outcome of colon adenocarcinoma through JNK pathways. *Oncotarget.* 2017;8(35):58611-58624. doi:10.18632/oncotarget.17381
- Guo C, Li S, Liang A, Cui M, Lou Y, Wang H. PPA1 promotes breast cancer proliferation and metastasis through PI3K/AKT/GSK3 $\beta$  signaling pathway. *Front Cell Dev Biol.* 2021;9:730558. doi:10.3389/fcell.2021.730558
- Cong L, Ran FA, Cox D, et al. Multiplex genome engineering using CRISPR/Cas systems. *Science.* 2013;339(6121):819-823. doi:10.1126/science.1231143
- Tomonaga T, Matsushita K, Yamaguchi S, et al. Identification of altered protein expression and post-translational modifications in primary colorectal cancer by using agarose two-dimensional gel electrophoresis. *Clin Cancer Res.* 2004;10(6):2007-2014. doi:10.1158/1078-0432.ccr-03-0321
- Li L, Aruna null, Luo D, Jin A. Clinical significance and functional validation of inorganic pyrophosphatase in diffuse large B cell lymphoma in humans. *Cytotechnology.* 2018;70(2):641-649. doi:10.1007/s10616-017-0165-5
- Chen G, Gharib TG, Huang CC, et al. Proteomic analysis of lung adenocarcinoma: identification of a highly expressed set of proteins in tumors. *Clin Cancer Res.* 2002;8(7):2298-2305.
- Kachman MT, Wang H, Schwartz DR, Cho KR, Lubman DM. A 2-D liquid separations/mass mapping method for interlysate comparison of ovarian cancers. *Anal Chem.* 2002;74(8):1779-1791. doi:10.1021/ac011159c
- Lexander H, Palmberg C, Auer G, et al. Proteomic analysis of protein expression in prostate cancer. *Anal Quant Cytol Histol.* 2005;27(5):263-272.
- Megger DA, Bracht T, Kohl M, et al. Proteomic differences between hepatocellular carcinoma and nontumorous liver tissue investigated by a combined gel-based and label-free quantitative proteomics study. *Mol Cell Proteom.* 2013;12(7):2006-2020. doi:10.1074/mcp.M113.028027
- Mishra DR, Chaudhary S, Krishna BM, Mishra SK. Identification of critical elements for regulation of inorganic pyrophosphatase (PPA1) in MCF7 breast cancer cells. *PLOS ONE.* 2015;10(4):e0124864. doi:10.1371/journal.pone.0124864
- Jeong SH, Ko GH, Cho YH, et al. Pyrophosphatase overexpression is associated with cell migration, invasion, and

- poor prognosis in gastric cancer. *Tumor Biol.* 2012;33(6): 1889-1898. doi:10.1007/s13277-012-0449-5
23. Yang Y, Cai J, Yin J, et al. Inorganic pyrophosphatase (PPA1) is a negative prognostic marker for human gastric cancer. *Int J Clin Exp Pathol.* 2015;8(10):12482-12490.
24. Xu D, Miao Y, Gu X, Wang J, Yu G. Pyrophosphatase 1 expression is associated with future recurrence and overall survival in Chinese patients with intrahepatic cholangiocarcinoma. *Oncol Lett.* 2018;15(5):8095-8101. doi:10.3892/ol.2018.8278
25. Niu H, Zhou W, Xu Y, et al. Silencing PPA1 inhibits human epithelial ovarian cancer metastasis by suppressing the Wnt/ $\beta$ -Catenin signaling pathway. *Oncotarget.* 2017;8(44): 76266-76278. doi:10.18632/oncotarget.19346
26. Luo D, Liu D, Shi W, et al. PPA1 promotes NSCLC progression via a JNK- and TP53-Dependent manner. *Oncogenesis.* 2019;8(10):53. doi:10.1038/s41389-019-0162-y
27. Li H, Xiao N, Li Z, Wang Q. Expression of inorganic pyrophosphatase (PPA1) correlates with poor prognosis of epithelial ovarian cancer. *Tohoku J Exp Med.* 2017;241(2): 165-173. doi:10.1620/tjem.241.165
28. Luo D, Wang G, Shen W, et al. Clinical significance and functional validation of PPA1 in various tumors. *Cancer Med.* 2016;5(10):2800-2812. doi:10.1002/cam4.894
29. Soleimani M, Somma A, Kaoud T, et al. Covalent JNK inhibitor, JNK-IN-8, suppresses tumor growth in triple-negative breast cancer by activating TFEB- and TFE3-mediated lysosomal biogenesis and autophagy. *Mol Cancer Ther.* 2022;21(10): 1547-1560. doi:10.1158/1535-7163.MCT-21-1044
30. Kojima T, Kato K, Hara H, et al. Phase II study of BKM120 in patients with advanced esophageal squamous cell carcinoma (EPOC1303). *Esophagus.* 2022;19(4):702-710. doi:10.1007/s10388-022-00928-3
31. Shrestha Bhattarai T, Shamu T, Gorelick AN, et al. AKT mutant allele-specific activation dictates pharmacologic sensitivities. *Nat Commun.* 2022;13(1):2111. doi:10.1038/s41467-022-29638-1
32. Volkamer A, Kuhn D, Rippmann F, Rarey M. DoGSiteScorer: a web server for automatic binding site prediction, analysis and druggability assessment. *Bioinformatics.* 2012;28(15): 2074-2075. doi:10.1093/bioinformatics/bts310
33. Dallakyan S, Olson AJ. Small-molecule library screening by docking with PyRx. *Meth Molecular Biol.* 2015;1263:243-250. doi:10.1007/978-1-4939-2269-7\_19
34. Sterling T, Irwin JJ. ZINC 15--Ligand discovery for everyone. *J Chem Inf Model.* 2015;55(11):2324-2337. doi:10.1021/acs.jcim.5b00559
35. Berman HM, Battistuz T, Bhat TN, et al. The protein data bank. *Acta Crystallogr D.* 2002;58(Pt 6No):899-907. doi:10.1107/s09074444902003451
36. Niu H, Zhu J, Qu Q, Zhou X, Huang X, Du Z. Crystallographic and modeling study of the human inorganic pyrophosphatase 1: A potential anti-cancer drug target. *Proteins: Struct, Funct, Bioinf.* 2021;89(7):853-865. doi:10.1002/prot.26064
37. Šali A, Blundell TL. Comparative protein modelling by satisfaction of spatial restraints. *J Mol Biol.* 1993;234(3): 779-815. doi:10.1006/jmbi.1993.1626
38. Shen M, Sali A. Statistical potential for assessment and prediction of protein structures. *Prot Sci.* 2006;15(11): 2507-2524. doi:10.1110/ps.062416606
39. Wiederstein M, Sippl MJ. ProSA-Web: interactive web service for the recognition of errors in three-dimensional structures of proteins. *Nucleic Acids Res.* 2007;35(Web Server issue): W407-W410. doi:10.1093/nar/gkm290
40. Laskowski RA, MacArthur MW, Moss DS, Thornton JM. PROCHECK: A program to check the stereochemical quality of protein structures. *J Appl Crystal.* 1993;26(2):283-291. doi:10.1107/S0021889892009944
41. Trott O, Olson AJ. AutoDock vina: improving the speed and accuracy of docking with a new scoring function, efficient optimization, and multithreading. *J Comput Chem.* 2010;31(2): 455-461. doi:10.1002/jcc.21334
42. Daina A, Michielin O, Zoete V. SwissADME: A free web tool to evaluate pharmacokinetics, drug-likeness and medicinal chemistry friendliness of small molecules. *Sci Rep.* 2017;7:42717. doi:10.1038/srep42717
43. Cheng F, Li W, Zhou Y, et al. AdmetSAR: a comprehensive source and free tool for assessment of chemical ADMET properties. *J Chem Inf Model.* 2012;52(11):3099-3105. doi:10.1021/ci300367a
44. Yang H, Lou C, Sun L, et al. AdmetSAR 2.0: web-service for prediction and optimization of chemical ADMET properties. *Bioinformatics.* 2019;35(6):1067-1069. doi:10.1093/bioinformatics/bty707
45. Lipinski CA, Lombardo F, Dominy BW, Feeney PJ. Experimental and computational approaches to estimate solubility and permeability in drug discovery and development settings. *Adv Drug Deliv Rev.* 2001;46(1-3):3-26. doi:10.1016/s0169-409x(00)00129-0
46. Muegge I, Heald SL, Brittelli D. Simple selection criteria for drug-like chemical matter. *J Med Chem.* 2001;44(12): 1841-1846. doi:10.1021/jm015507e
47. Benet LZ, Hosey CM, Ursu O, Oprea TI. BDDCS, the rule of 5 and drugability. *Adv Drug Deliv Rev.* 2016;101:89-98. doi:10.1016/j.addr.2016.05.007
48. Martin YC. A bioavailability score. *J Med Chem.* 2005;48(9): 3164-3170. doi:10.1021/jm0492002
49. Shen J, Cheng F, Xu Y, Li W, Tang Y. Estimation of ADME properties with substructure pattern recognition. *J Chem Inf Model.* 2010;50(6):1034-1041. doi:10.1021/ci100104j
50. Zhu H, Martin TM, Ye L, Sedykh A, Young DM, Tropsha A. Quantitative structure-activity relationship modeling of rat acute toxicity by oral exposure. *Chem Res Toxicol.* 2009;22(12): 1913-1921. doi:10.1021/tx900189p
51. Abraham MJ, Murtola T, Schulz R, et al. GROMACS: high performance molecular simulations through multi-level parallelism from laptops to supercomputers. *SoftwareX.* 2015;1-2: 19-25. doi:10.1016/j.softx.2015.06.001
52. Lindorff-Larsen K, Piana S, Palmo K, et al. Improved side-chain torsion potentials for the amber ff99SB protein force field: improved protein Side-Chain potentials. *Proteins: Struct, Funct, Bioinf.* 2010;78(8):1950-1958. doi:10.1002/prot.22711
53. Sheik Amamuddy O, Musyoka TM, Boateng RA, Zabo S, Tasthan Bishop Ö. Determining the unbinding events and conserved motions associated with the pyrazinamide release due to resistance mutations of mycobacterium tuberculosis pyrazinamidase. *Comput Struct Biotechnol J.* 2020;18: 1103-1120. doi:10.1016/j.csbj.2020.05.009



54. Martoňák R, Laio A, Parrinello M. Predicting crystal structures: the Parrinello-Rahman method revisited. *Phys Rev Lett*. 2003;90(7):075503. doi:10.1103/PhysRevLett.90.075503
55. Hess B, Bekker H, Berendsen HJC, Fraaije JGEM. LINCS: a linear constraint solver for molecular simulations. *J Comput Chem*. 1997;18(12):1463-1472. doi:10.1002/(SICI)1096-987X(199709)18:12<1463::AID-JCC4>3.0.CO;2-H
56. Kabsch W, Sander C. Dictionary of protein secondary structure: pattern recognition of hydrogen-bonded and geometrical features. *Biopolymers*. 1983;22(12):2577-2637. doi:10.1002/bip.360221211
57. Touw WG, Baakman C, Black J, et al. A series of PDB-related databanks for everyday needs. *Nucleic Acids Res*. 2015;43(Database issue):D364-D368. doi:10.1093/nar/gku1028
58. Brown DK, Penkler DL, Sheik Amamuddy O, et al. MD-TASK: a software suite for analyzing molecular dynamics trajectories. *Bioinformatics*. 2017;33(17):2768-2771. doi:10.1093/bioinformatics/btx349
59. Eriksson P, Marzouka N, Sjö Dahl G, Bernardo C, Liedberg F, Höglund M. A comparison of rule-based and centroid single-sample multiclass predictors for transcriptomic classification. *Bioinformatics*. 2022;38(4):1022-1029. doi:10.1093/bioinformatics/btab763
60. Bhardwaj VK, Oakley A, Purohit R. Mechanistic behavior and subtle key events during DNA clamp opening and closing in T4 bacteriophage. *Int J Biol Macromol*. 2022;208:11-19. doi:10.1016/j.ijbiomac.2022.03.021
61. Kumar Bhardwaj V, Purohit R, Kumar S. Himalayan bioactive molecules as potential entry inhibitors for the human immunodeficiency virus. *Food Chem*. 2021;347:128932. doi:10.1016/j.foodchem.2020.128932
62. Miller BR, McGee TD, Swails JM, Homeyer N, Gohlke H, Roitberg AE. MMPBSA.py: an efficient program for end-state free energy calculations. *J Chem Theory Comput*. 2012;8(9):3314-3321. doi:10.1021/ct300418h
63. Valdés-Tresanco MS, Valdés-Tresanco ME, Valiente PA, Moreno E. Gmx\_MMPBSA: a new tool to perform end-state free energy calculations with GROMACS. *J Chem Theory Comput*. 2021;17(10):6281-6291. doi:10.1021/acs.jctc.1c00645
64. Kumar S, Kumar S. Molecular docking: a structure-based approach for drug repurposing. In *Silico Drug Design*. Elsevier; 2019:161-189.
65. Guan L, Yang H, Cai Y, et al. ADMET-Score—a comprehensive scoring function for evaluation of chemical drug-likeness. *MedChemComm*. 2019;10(1):148-157. doi:10.1039/c8md00472b
66. Wallace AC, Laskowski RA, Thornton JM. LIGPLOT: a program to generate schematic diagrams of protein-ligand interactions. *Protein Eng*. 1995;8(2):127-134. doi:10.1093/protein/8.2.127
67. Arnittali M, Rissanou AN, Harmandaris V. Structure of biomolecules through molecular dynamics simulations. *Procedia Com Sci*. 2019;156:69-78. doi:10.1016/j.procs.2019.08.181
68. David CC, Jacobs DJ. Principal component analysis: a method for determining the essential dynamics of proteins. *Meth Mol Biol*. 2014;1084:193-226. doi:10.1007/978-1-62703-658-0\_11
69. Papaleo E, Mereghetti P, Fantucci P, Grandori R, De Gioia L. Free-energy landscape, principal component analysis, and structural clustering to identify representative conformations from molecular dynamics simulations: the myoglobin case. *J Mol Graph*. 2009;27(8):889-899. doi:10.1016/j.jmgm.2009.01.006
70. Arnold GE, Ornstein RL. Molecular dynamics study of time-correlated protein domain motions and molecular flexibility: cytochrome P450BM-3. *Biophys J*. 1997;73(3):1147-1159. doi:10.1016/S0006-3495(97)78147-5
71. Abbruzzese JL, Gholson CF, Daugherty K, et al. A pilot clinical trial of the cholecystokinin receptor antagonist MK-329 in patients with advanced pancreatic cancer. *Pancreas*. 1992;7(2):165-171. doi:10.1097/00006676-199203000-00006
72. Zabielski R, Leśniewska V, Borlak J, et al. Effects of intraduodenal administration of tarazepide on pancreatic secretion and duodenal EMG in neonatal calves. *Regul Pept*. 1998;78(1-3):113-123. doi:10.1016/S0167-0115(98)00139-6
73. Naritomi Y, Terashita S, Kagayama A, Sugiyama Y. Utility of hepatocytes in predicting drug metabolism: comparison of hepatic intrinsic clearance in rats and humans in vivo and in vitro. *Drug Metab Dispos*. 2003;31(5):580-588. doi:10.1124/dmd.31.5.580
74. Okayama Y, Hiroi J, Lau LCK, Church MK. Inhibition of histamine and eicosanoid release from dispersed human lung cells in vitro by quinotolast. *Jpn J Pharmacol*. 1995;69(4):375-380. doi:10.1254/jjp.69.375
75. Wolber G, Langer T. LigandScout: 3-D pharmacophores derived from protein-bound ligands and their use as virtual screening filters. *J Chem Inf Model*. 2005;45(1):160-169. doi:10.1021/ci049885e
76. Yang SY. Pharmacophore modeling and applications in drug discovery: challenges and recent advances. *Drug Discov Today*. 2010;15(11-12):444-450. doi:10.1016/j.drudis.2010.03.013
77. Chen D, Oezguen N, Urvil P, Ferguson C, SMM, Dann, Savidge TC. Regulation of protein-ligand binding affinity by hydrogen bond pairing. *Sci Adv*. 2016;2(3):e1501240. doi:10.1126/sciadv.1501240
78. Berlin RG, Freidinger RM. Characterization of MK-329. In: Adler G, Beglinger C, eds. *Cholecystokinin Antagonists in Gastroenterology*. Springer Berlin Heidelberg; 1991:70-79.
79. Kobayashi K, Hiroi J, Kishi S, et al. Effects of quinotolast, a new orally active antiallergic drug, on experimental allergic models. *Jpn J Pharmacol*. 1993;63(1):73-81. doi:10.1254/jjp.63.73
80. Meltzer E. Performance effects of antihistamines. *J Allergy Clin Immunol*. 1990;86(4):613-619. doi:10.1016/S0091-6749(05)80225-8
81. Zamani F, Zamani N, Suzuki T, Doustkhah E. Biological behavior of 1,4-benzodiazepines and 1,4-benzothiazepines. In *Benzodiazepine-Based Drug Discovery*. Elsevier; 2022:77-124.
82. Dehury B, Behera SK, Mahapatra N. Structural dynamics of casein kinase I (CKI) from malarial parasite plasmodium falciparum (Isolate 3D7): insights from theoretical modelling and molecular simulations. *J Mol Graph*. 2017;71:154-166. doi:10.1016/j.jmgm.2016.11.012
83. Prahara AB, Dehury B, Mahapatra N, Kar SK, Behera SK. Molecular dynamics insights into the structure, function, and substrate binding mechanism of mucin desulfating sulfatase of gut microbe *Bacteroides Fragilis*. *JCB*. 2018;119(4):3618-3631. doi:10.1002/jcb.26569

84. Rout M, Dey S, Mishra S, et al. Machine learning and classical MD simulation to identify inhibitors against the P37 envelope protein of monkeypox virus. *J Biomol Struct Dyn*. Published online May 23, 2023;1-14. doi:10.1080/07391102.2023.2216290
85. Rout M, Mishra S, Dey S, Singh MK, Dehury B, Pati S. Exploiting the potential of natural polyphenols as antivirals against monkeypox envelope protein F13 using machine learning and all-atoms MD simulations. *Comput Biol Med*. 2023;162:107116. doi:10.1016/j.compbimed.2023.107116

## SUPPORTING INFORMATION

Additional supporting information can be found online in the Supporting Information section at the end of this article.

**How to cite this article:** Menteş M, Yandım C. Identification of PPA1 inhibitor candidates for potential repurposing in cancer medicine. *J Cell Biochem*. 2023;124:1646-1663. doi:10.1002/jcb.30475